sustainability

Article

Study on the Mechanisms of Rock Mass Watering for Rockburst Prevention in Phosphorite Mines from Laboratory Results

Meng Wu [1], Yicheng Ye [1,2], Qihu Wang [1,2,*], Zhen Zhang [1], Yan Li [1] and Wen Li [3]

1 School of Resources and Environmental Engineering, Wuhan University of Science and Technology, Wuhan 430081, China; wumeng@wust.edu.cn (M.W.); yeyicheng@wust.edu.cn (Y.Y.); zhangzh0504@163.com (Z.Z.); 18335570015@163.com (Y.L.)
2 Industrial Safety Engineering Technology Research Center of Hubei Province, Wuhan University of Science and Technology, Wuhan 430081, China
3 School of Architectural Engineering, Huanggang Normal University, Huanggang 438000, China
* Correspondence: wangqihu@wust.edu.cn; Tel.: +86-027-6886-2885

Abstract: Owing to the continuous increase in mining depth, Yichang phosphorite mines in China have entered the field of deep mining. The frequency of rockburst disasters is increasing. In situ experience indicates that the practice of spraying water onto a working face after blasting is an effective method of rockburst prevention. In order to investigate the underlying mechanisms of rockburst prevention by watering in phosphorite mines, a series of uniaxial compression laboratory experiments was carried on phosphorite samples under dry and water-saturated conditions with an acoustic emission (AE) monitoring system. A high-speed camera was used to record the failure process and pattern of a given rock sample prior to rockburst. The effects of water on the mechanical properties and fracturing characteristics of phosphorite failure were determined. Experimental results indicate that water reduces the uniaxial compressive strength and Young's modulus. Saturated phosphorite causes more small fragments after it fractures. A Gaussian mixture model (GMM) clustering algorithm was utilized to analyze the crack propagation patterns of rock samples during the entire process. It was determined that during the unstable crack propagation phase, the presence of water makes the shear characteristics become more obvious. Water reduces releasable strain energy which is consumed by internal damage and plastic deformation of the rock sample. Moreover, the mechanism of watering for rockburst prevention is discussed from both macro and micro perspectives. The primary reasons for this are the transfer of stress concentration zones and stress-releasing effects via microcrack propagation on the working face.

Keywords: rockburst prevention; rock mass watering; Yichang phosphorite mining; stress concentration zone; microcrack propagation

check for updates

Citation: Wu, M.; Ye, Y.; Wang, Q.; Zhang, Z.; Li, Y.; Li, W. Study on the Mechanisms of Rock Mass Watering for Rockburst Prevention in Phosphorite Mines from Laboratory Results. *Sustainability* **2023**, *15*, 9010. https://doi.org/10.3390/su15119010

Academic Editor: Kaihui Li

Received: 18 March 2023
Revised: 29 May 2023
Accepted: 31 May 2023
Published: 2 June 2023

1. Introduction

Rockburst is among the most dangerous dynamic hazards in deep mines and tunnels [1]. It is a violent rupture of rock mass accompanied with a sharp release of stored elastic energy and a rapid ejection of rock fragments [2]. The failure mode of the surrounding rock can be changed from superficial spalling to violent rockburst as the depth increases [3]. Many mines and tunnels have suffered from rockburst due to its abrupt, stochastic, unpredictable and destructive nature [4]. In order to reveal the mechanism of rockburst, many scholars have conducted a series of studies on the mechanism of rockburst [5–10]. Li illustrated that internal pre-static stress is the dominant factor for rock failure and that external dynamic disturbance stress is an important inducement [11]. Deng and Su pointed out that induced rockbursts are essentially nonlinear phenomena and set up the quantitative relationship between blasting parameters and rockbursts [12].

Meanwhile, studies on the prevention and control of rockburst are also of great significance [13–16]. Field and laboratory experiments show that spraying water onto or injecting it into the heading face can effectively reduce the frequency and severity of rockburst. Rocks exhibit significant differences in mechanical behavior under saturated water and dry conditions [17]. Many studies focus on water–rock interactions in order to analyze the influence of water content on mechanical properties and failure mode [18–28]. For instance, Erguler and Ulusay highlighted the negative exponential relationship between uniaxial compressive strength of rock and water content [29]. Waza et al. focused on the influence of water on rock crack propagation. Crack propagation velocity increases dramatically with increasing water content in clay-bearing rocks [30]. Nara et al. illustrated that the crack propagation velocity increases dramatically with increasing water content in granite [31]. Xie et al. focused on the damage evolution and control mechanisms of rock mechanical behavior in the Three Gorges Reservoir area. It has been reported previously that the dissolution and microcracks of carbonate cement in sandstone may be the main reasons for damage [20]. However, Wong et al. pointed out, through a summary of the literature, that water content is not the only factor affecting rock strength and modulus. In fact, porosity, density and strain rate are also significant factors [32].

In deep hard-rock tunnels, there is generally no rockburst when the surrounding rock is rich in water; however, relatively dry rock mass is prone to rockburst [33]. Water content exhibits a significant effect on the mechanical behavior of surrounding rock. Therefore, some researchers have studied the impact of water on rockburst and coal bump [34–39]. Varied water content changes the fracturing pattern of tunnel-surrounding rock, making it more prone to shear fracturing under saturated conditions and forming a wider and deeper "V" shaped fracture zone. Conversely, under dry conditions, the fracture pattern exhibits a typical layered fracture mode. High water content will cause the surrounding rock to exhibit a lower dynamic failure rate and faster static failure [40]. Luo performed a study on uniaxial and true triaxial compression tests of natural and saturated red sandstone. It has been reported that red sandstone in a saturated state has a more obvious shear effect. Water affects the meso mechanism of rock spalling. One study highlighted that the prevention mechanism behind the application of water onto rockburst involves a reduction in the residual elastic strain energy and avoiding the excessive concentration of strain energy [41]. Luo conducted a series of true triaxial tests on natural and saturated red sandstone samples containing D-shaped holes in order to study the effect of water on rockburst in D-shaped tunnels. Water was found to reduce the capacity of surrounding rock to store elastic strain energy, and increase the dissipated energy required for deformation and failure [42]. Cai carried out a series of uniaxial compression tests on sandstone to study the mechanism of watering in order to prevent rockburst. He pointed out that the decrease in rock energy storage capacity and the decrease in stress near the working face are the main reasons for rockburst being avoided [43].

Numerous investigations have shown that rockburst usually occurs in brittle, hard rocks under high levels of geological stress [11,44,45], and that its hazards increase significantly with the increase in mining depth. Yichang, China, is rich in phosphorite resources, with most of the area's multi-billion-ton phosphorite resources buried at a depth of 500–800 m and, with additional resources found at depths greater than 1000 m. Rockburst disasters are gradually becoming more serious. Figure 1 shows the phosphorite mines in Yichang, an area where rockburst is serious. Figure 2 shows the rockburst and its support near the working face. Therefore, in order to more effectively prevent rockbursts, it is important to study the mechanisms involved in rock mass watering for rockburst prevention in phosphorite mines.

This study aims to deduce the mechanism behind watering for the purposes of preventing rockburst in phosphorite mines and of enhancing our understanding of damage evolution in phosphorite. For this purpose, we have carried out uniaxial compression tests on phosphorite under dry and saturated conditions and used high-speed cameras to record the failure process in order to analyze the effect of water on mechanical properties. At the same time, an acoustic emission system was used to reveal the damage evolution in dry and saturated phosphorite via a process of acoustic characterization.

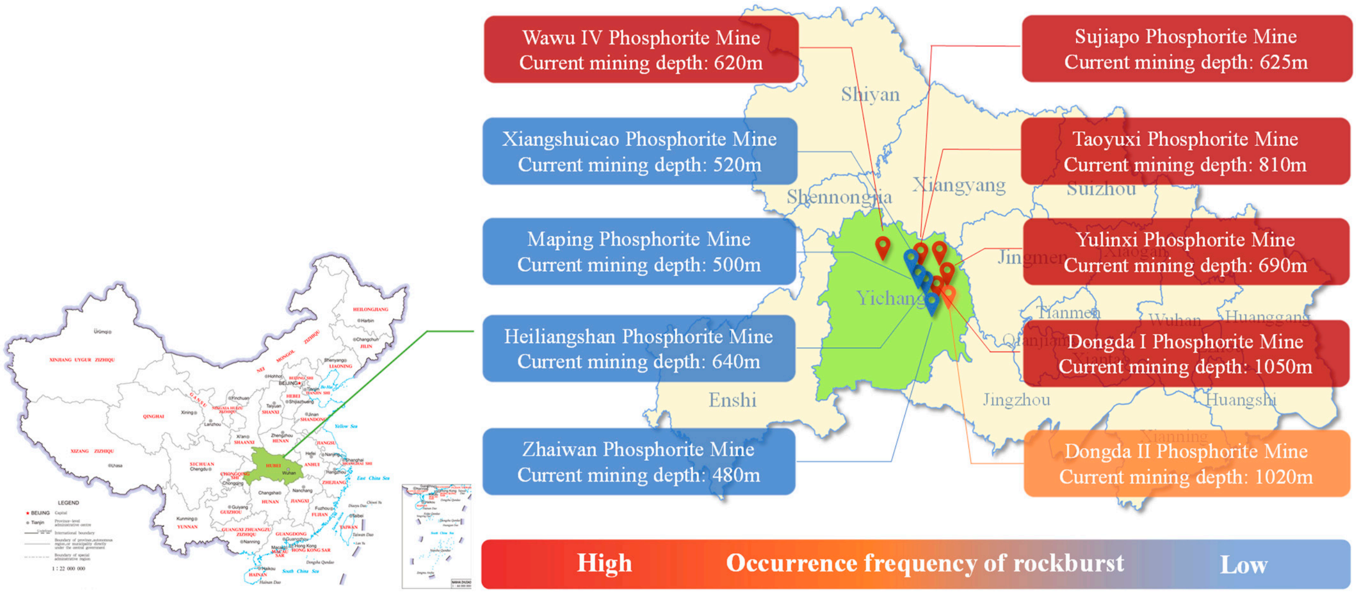

Figure 1. Typical phosphorite mines with rockburst in Yichang area.

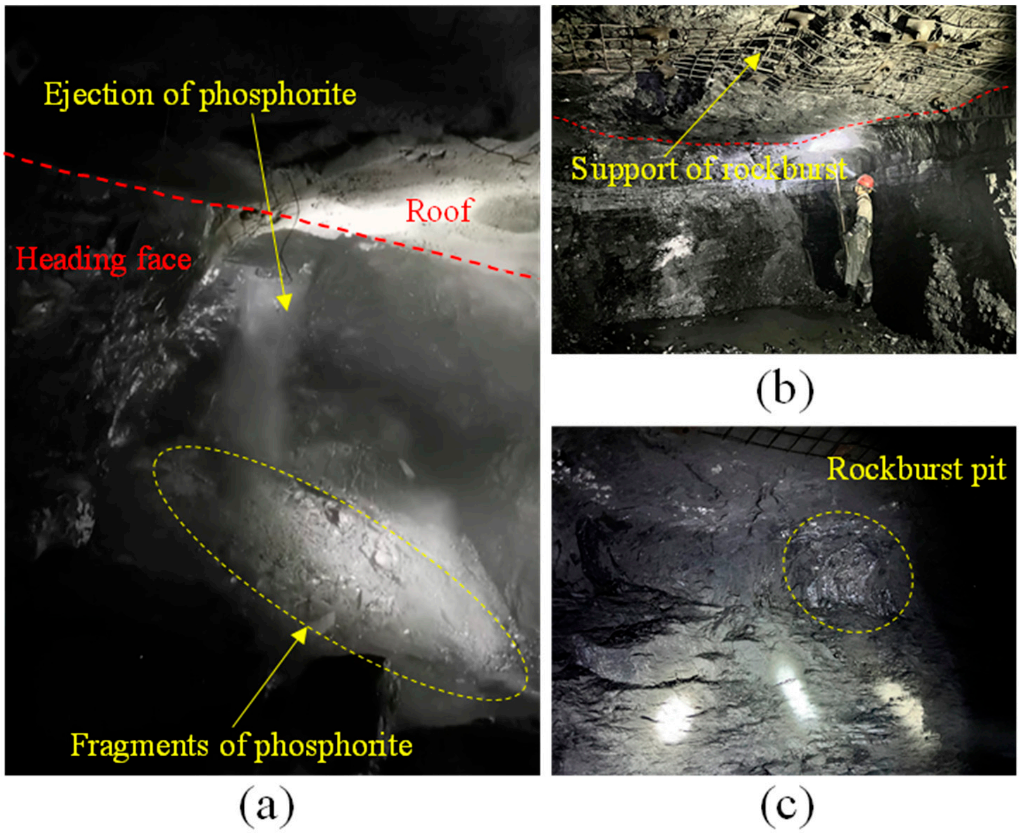

Figure 2. Photographs of rockburst at working face: (**a**) Rock bursting; (**b**) Support of rockburst; (**c**) Rockburst pit.

2. Experiments

2.1. Rock Material and Sample Preparation

All phosphorite samples were taken near the working face buried at a depth of 800 m in the Yichang Dongda Mine, China. Samples of typical phosphorite extracted from rockburst-prone sites were selected for core drilling at depths of 600 m to 1000 m, as shown in Figure 3. Physical parameters were measured, as shown in Table 1. All samples were taken perpendicularly to the bedding surface, with a diameter of 50 mm and a length of 100 mm [46]. The samples include two groups: dry and saturated. Each group includes 3 rock samples. Dry samples were dried at temperature of 105 °C for 12 h. Saturated samples were soaked in distilled water and weighed every 2 h until the weight stopped changing.

Figure 3. Phosphorite samples: (**a**) phosphorite core; (**b**) experimental samples.

Table 1. Main physical parameters of the phosphorite.

Simple No.	Density (g/cm^3)	Connected Porosity (%)	P-Wave Velocity (m/s)
S01	2.829	0.524	4526
S02	2.912	0.581	4125
S03	2.575	0.538	4423
S04	2.682	0.556	4418
S05	2.591	0.541	4483
S06	2.722	0.573	4674

2.2. Experimental Methodology

The apparatuses used in uniaxial compression experiments are displayed in Figure 4. During the test, axial load was applied at an axial displacement rate of 0.004 mm/s, and both axial load and displacement were recorded at a sampling interval of 0.2 s. A 16-channel AE signal monitoring system was used to record the AE signal of the sample during loading. Two AE sensors were directly fixed to the rock surface with transparent tape, and a thin layer of Vaseline was applied between the sample and the sensor to provide good acoustic coupling. During the monitoring process, a gain effect of 40 dB was selected for the AE signals, and the trigger threshold was set to 40 dB in order to filter the background noise.

A high-speed camera (see Figure 4) was applied to the loading system in order to record the fracturing process of rock samples. A transparent acrylic plate was used to prevent any damage caused by the ejection of phosphorite fragments.

Due to the limitations of camera memory, we focused on capturing the fracturing evolution observable near the peak stress. The frame rate of camera was set to 40,000 fps.

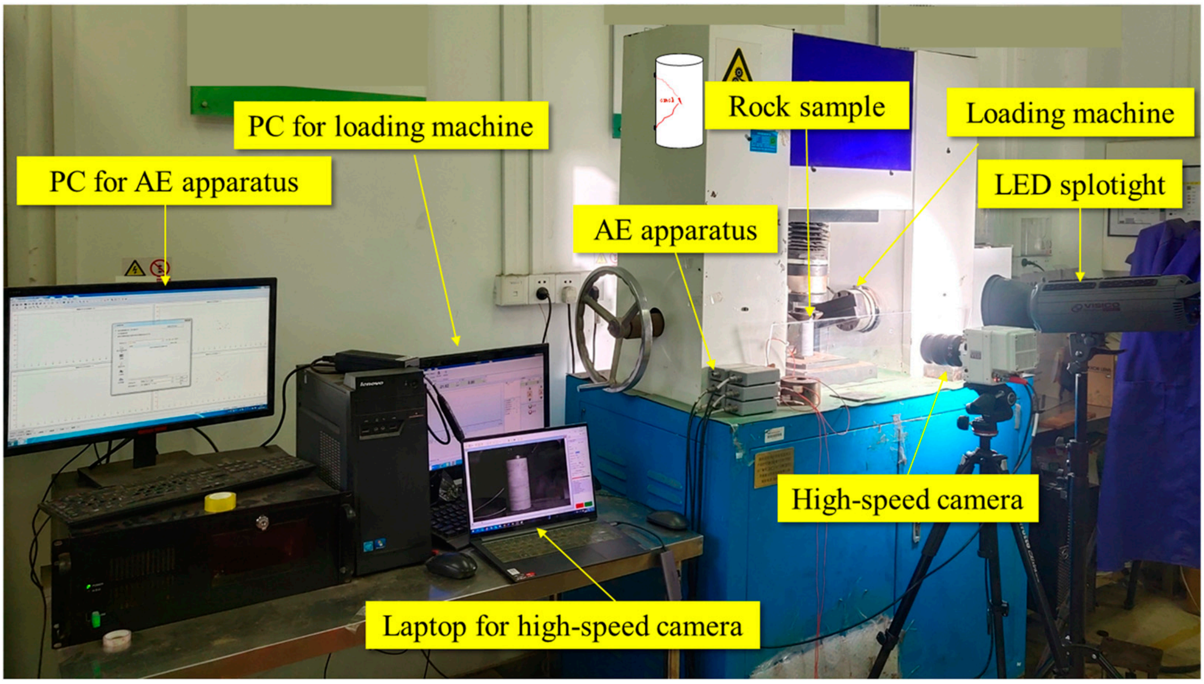

Figure 4. Experimental setup.

3. Analysis of Experimental Results

3.1. Stress–Strain Curves

Figure 5 shows the stress–strain curves of phosphorite in dry and saturated states. When the stress reached its peak level, the rock sample was found to be completely fractured and possess no residual strength. Compared with saturated phosphorite, dry phosphorite has a higher peak stress and steeper slope in the elastic region.

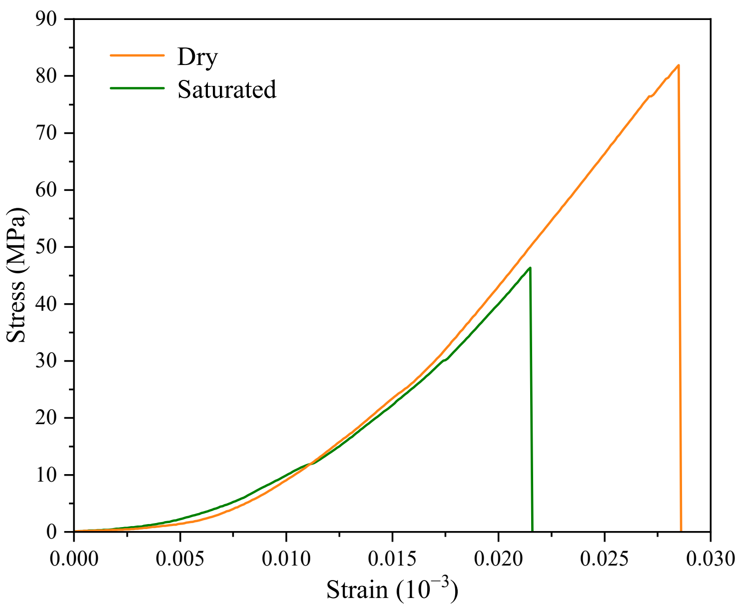

Figure 5. Stress–strain curves under dry and saturated conditions.

Table 2 shows the mechanical parameters and reduction due to the application ofwater to phosphorite, including uniaxial compressive strength (*UCS*) and Young's modulus (*E*).

Table 2. Values of phosphorite mechanical properties.

Simple No.	Moisture State	*UCS* (MPa)	*E* (GPa)	Percentage Reduction Due to Water	
				UCS	*E*
S01	Dry	81.64	4.61		
S02		76.86	4.26		
S03		86.29	4.37		
S04	Saturated	50.16	3.92	38.56%	14.97%
S05		45.83	4.04	40.37%	5.16%
S06		51.47	3.86	40.35%	11.67%

Table 2 indicates that water significantly weakens the uniaxial compressive strength *UCS* of phosphorite. The percentage reduction that occurred due to water can be calculated as:

$$\begin{aligned}&\text{Percentage Reduction of } UCS = (UCS_{\text{dry}} - UCS_{\text{saturated}})/UCS_{\text{dry}}\\&\text{Percentage Reduction of } E = (E_{\text{dry}} - E_{\text{saturated}})/E_{\text{dry}}\end{aligned} \quad (1)$$

The average reductions of *UCS* and *E* are 39.76% and 10.66%, respectively.

3.2. Fracturing Process and Failure Pattern of Dry and Saturated Phosphorite

Figures 6 and 7 show the process from the first observation of macroscopic cracks until the complete fracturing of samples. The first frame is the initial state of the sample without loading. The second frame is the time (0 s) from the start of loading for the first macroscopic cracks of the sample. The time on the subsequent frames is the time interval from the initiation of cracking.

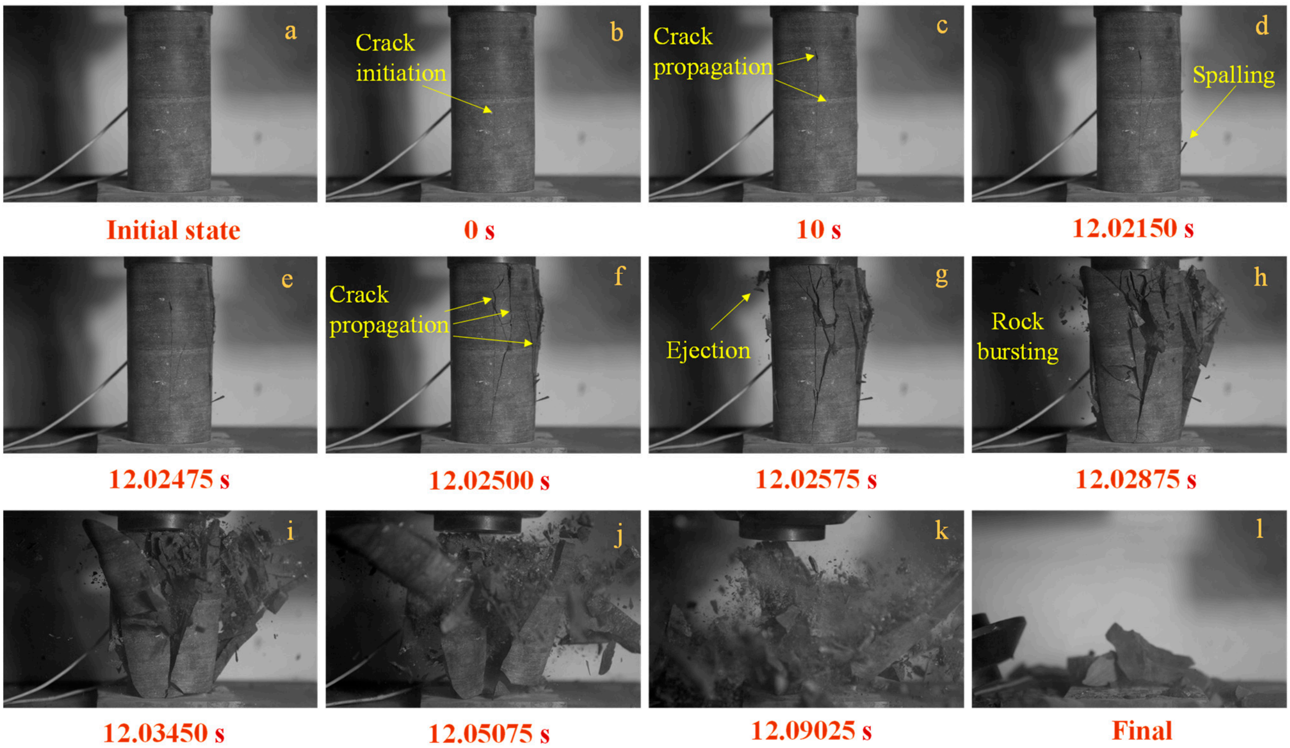

Figure 6. Selected representative frames showing fracturing processes of dry phosphorite: (**a**) Initial state; (**b**) At 0 s; (**c**) At 10 s; (**d**) At 12.02150 s; (**e**) At 12.02475 s; (**f**) At 12.02500 s; (**g**) At 12.02575 s; (**h**) At 12.05875 s; (**i**) At 12.03450 s; (**j**) At 12.05075 s; (**k**) At 12.09025 s; (**l**) Final state.

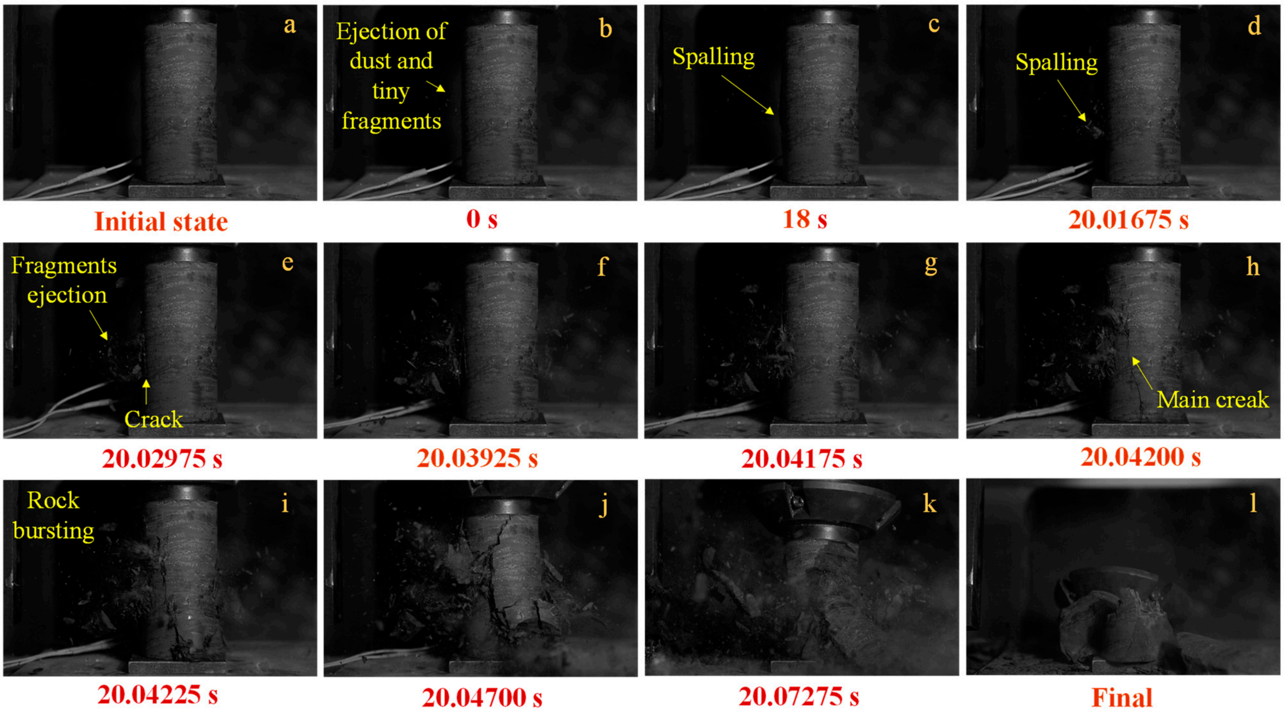

Figure 7. Selected representative frames showing fracturing processes of saturated phosphorite: (**a**) Initial state; (**b**) At 0 s; (**c**) At 18 s; (**d**) At 20.01675 s; (**e**) At 20.02975 s; (**f**) At 20.03925 s; (**g**) At 20.04175 s; (**h**) At 20.04200 s; (**i**) At 20.04225 s; (**j**) At 20.04700 s; (**k**) At 20.07275 s; (**l**) Final state.

Figure 6 shows the fracturing process of dry phosphorite under a uniaxial compression load. In Figure 6b, the first large axial tensile crack appears in the middle of the sample with a crackling sound. After a 10 s quiet period, the crack begins to grow (Figure 6c). During 12.02150 s–12.02475 s (Figure 6d,e), some small particles and fragments fall and are ejected from the surface of the sample, which can be understood as a light rockburst in-site. At 12.02555 s, the crack begins to expand to a large area (Figure 6f). At 12.02875 s, the whole sample completely fractures along the crack and splits into many large fragments, fine particles and powder, a moment accompanied by a loud bang (Figure 6h).

Figure 7 shows the fracturing process of dry phosphorite under uniaxial compression load. Figure 7b shows the ejection of fine particles and dust from the left surface of the sample with a slight sound. After a quiet period of 18 s, small fragments spall from the surface (Figure 7c). At 20.01675 s, some fragments are ejected (Figure 7d), followed by the emergence of large cracks (In Figure 7e). At 20.04200 s, a main crack (Figure 7h) appears on the surface of the sample, followed by severe fragmentation and a burst of powder accompanied by a violent bang (Figure 7i).

The failure patterns of dry and water-saturated phosphorites are shown in Figures 8 and 9. We can observe the following from the high-speed camera images captured and post-mortem samples:

Figure 8. The failure patterns and macro morphology of dry phosphorite.

Figure 9. The failure patterns and macro morphology of saturated phosphorite.

1. Both the dry and the saturated sample are violently fractured into multiple fragments, and tiny fragments and powder are rapidly ejected from the sample surface before rock bursting. The difference is that a significantly greater quantity of small fragments and powder are produced by the fracturing of the saturated sample than by the dry sample. There is speculation that water affects the crack propagation rate, resulting in greater numbers of small fragments appearing after the saturated sample fractures [30]. The results are opposite to those of red sandstone [43]. It is mainly due to differences in mineralogical composition, resulting in different effects of water.
2. The majority of fractures that occur in both dry and saturated samples are tensile. In the case saturated samples, however, there is a greater abundance of shear cracks. This

is probably due to the fact that when the rock pores are closed, the hole walls on both sides are in direct contact, and the existence of the bound water film on the surface of the mineral particles (weakly bound water has some of the properties of liquid water) reduces the friction and shear strength between the two, which is similar to the effect achieved by the addition of a lubricating layer between two elastic plates [47].

3.3. Evolution of Damage and AE Parameters during Loading Process

The evolution characteristics of AE hit rate and accumulated AE energy associated with the stress–strain curve under dry and saturated conditions were analyzed, and the results are shown in Figure 10. C1 and C2 divide the deformation and damage process into three phases:

1. Crack closure phase. In this phase, a small amount of AE signals is generated for dry samples, and the accumulated AE energy starts to grow slowly, while there is almost no AE signal generated for saturated samples in this phase, and the AE energy growth trend is not obvious. This phenomenon can be explained because in this phase, the stress level is relatively low, and the deformation of the sample occurs primarily due to the compaction and closure of the original microcracks within it. During the closure process, the rough surface is occluded and damaged, and some coarse particles are rubbed, resulting in the generation of a small amount of AE signals.
2. Linear-elastic deformation phase. In this phase, the AE rate of dry and saturated samples begins to increase gradually, and the accumulated AE energy also begins to increase rapidly. The AE rate and cumulative AE energy curve show a similar trend to that exhibited by the stress–strain curves. This phase is dominated by elastic deformation, with the occurrence of only limited plastic deformation.
3. Damage evolution phase. The damage accumulation in this phase contains the precursor information of the fracture. During this phase, the AE rate and accumulated AE energy of dry and saturated rock samples increase significantly, indicating that the initiation and propagation of cracks in this phase promote the generation of AE signals. As the load level approaches its peak, the microcracks in the sample begin to increase and gradually expand. The AE rate and accumulated AE energy increase sharply. The occurrence of fractures can be seen in both dry and saturated samples. The AE rate and accumulated AE energy of dry samples are lower than the same parameters of saturated samples, which are opposite to red sandstone [43].

In general, during the whole loading process, due to the presence of water, the AE rate and accumulated AE energy of dry samples are lower than those that of the saturated samples. Additionally, in the crack closure phase, the saturated rock sample has almost no AE signal, which may be due to the lubrication of water in the original microfracture, resulting in less fine particle friction in the process of fracture closure than that seen in the dry samples.

3.4. RA–AF Analysis of AE Parameters of Dry and Saturated Phosphorite

The RA–AF parametric analysis method proposed by the Japanese Construction Materials Standard (JCMS-III B5706) (2003) was used to study the RA–AF values during loading of phosphorite. The RA (rise time/maximum amplitude) value can be used to characterize the generation mechanism of AE sources; additionally, often when combined with the AF (average frequency) value, AF is used to analyze the failure pattern of rocks [48–51]. High RA values and low AF values indicate that the fracture at a certain point is of a shear type, while the low RA values and high AF values indicate that the fracture at a certain time is tensile in nature.

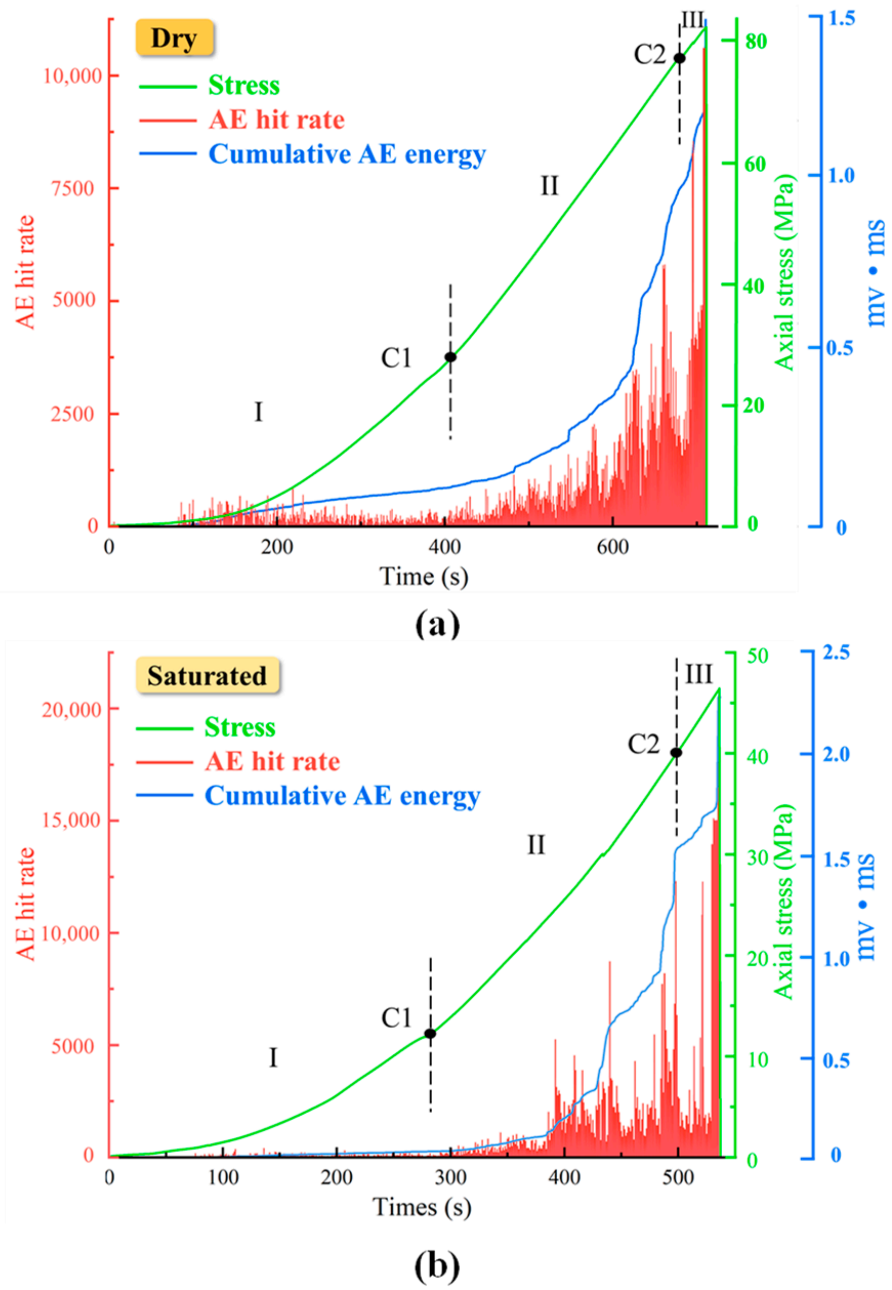

Figure 10. Evolution of AE hit rate and accumulated AE energy: (**a**) dry phosphorite; (**b**) saturated phosphorite.

The Gaussian mixed model (GMM) clustering algorithm is used to analyze RA–AF values, the basic idea being that multiple Gaussian probability density distributions are used to maximize the maximum likelihood probability of RA–AF data under the distribution outlined in [52–54]. Due to the relative independence and randomness of AE signal data, compared with the analysis method proposed by JCMS-III B5706, the probability of a GMM clustering algorithm simulating and fitting AE signal data is substantially higher. The Python program is applied to GMM cluster analysis in order to identify the crack type. Figure 11 shows the results of crack classification for dry and saturated phosphorite. The entire loading process is divided into 5 stages, including load levels of 0–20%, 20–40%, 40–60%, 60–80% and 80–100%. The results of the proportions of tensile and shear cracks in dry and saturated samples at each stage are shown in Table 3.

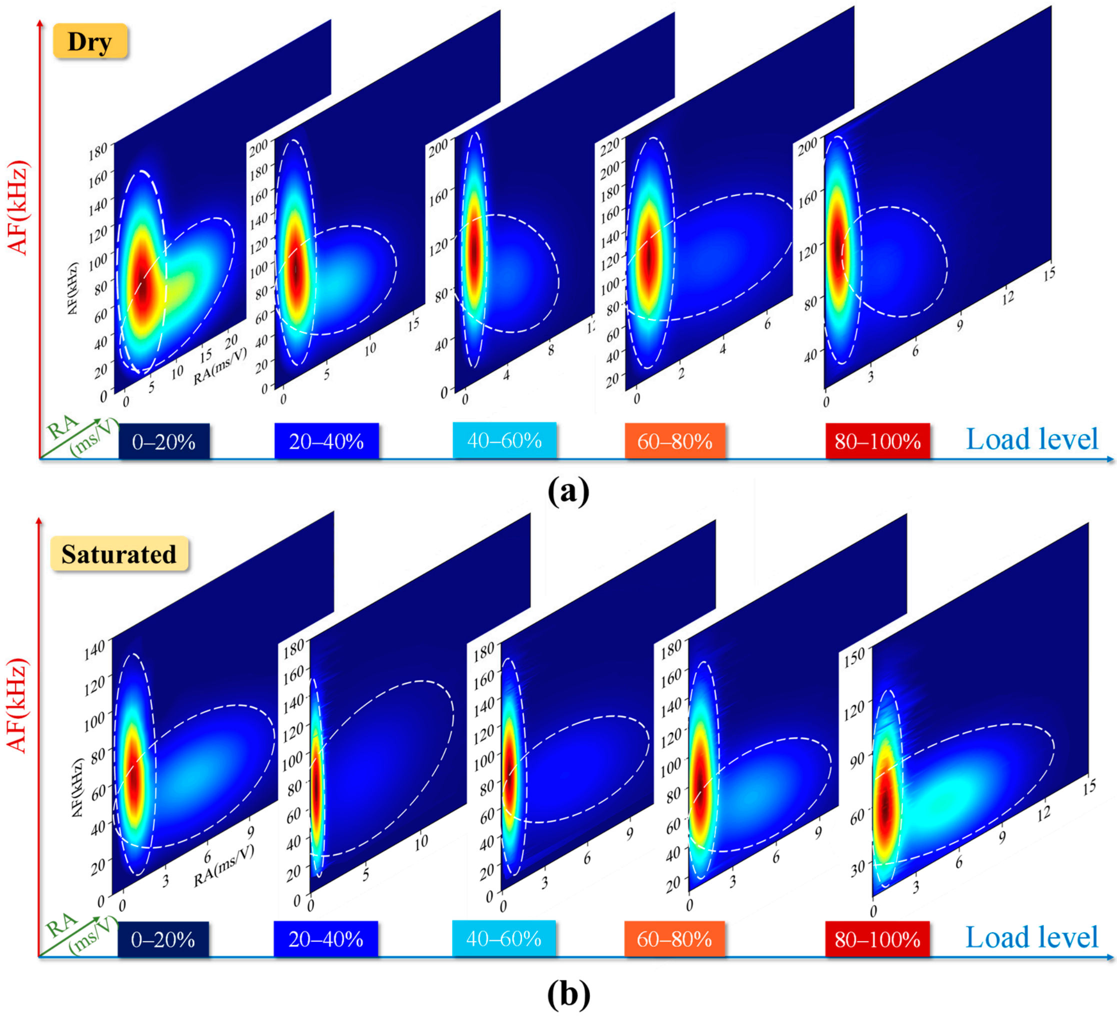

Figure 11. Contour map of GMM density at five stages of phosphorite: (**a**) dry; (**b**) saturated.

Table 3. Proportion of tensile and shear cracks at each stage in dry and saturated samples.

Load Level	Condition	Tensile (%)	Shear (%)	Tensile Average		Shear Average	
				RA (ms/V)	AF (10^2 kHz)	RA (ms/V)	AF (10^2 kHz)
0–20%	Dry	52.61	47.39	4.127	0.728	11.278	0.639
	Saturated	51.17	48.83	1.283	0.621	5.312	0.462
20–40%	Dry	58.63	41.37	2.475	0.914	7.538	0.635
	Saturated	52.31	47.69	0.514	0.752	7.695	0.713
40–60%	Dry	62.74	37.26	1.341	1.145	4.723	0.747
	Saturated	56.47	43.53	0.837	0.821	5.892	0.772
60–80%	Dry	58.84	41.16	0.852	1.163	4.184	1.087
	Saturated	54.46	45.54	0.721	0.784	0.462	0.473
80–100%	Dry	64.03	35.97	1.526	1.182	5.279	0.821
	Saturated	45.77	54.23	0.638	0.584	0.512	0.461

Figure 11 shows the contour map of GMM density, where the red area represents a higher probability density and the blue area represents a lower probability density. The tensile and shear crack areas are surrounded by dotted ellipses to a value twice the standard deviation ellipses of the Gaussian model, representing a confidence interval of 0.9 [55]. It can be seen that tensile cracks dominate the two states during the entire loading process, but that there are differences at each loading level. At the initial stage of loading (0–20%), the shear cracks of dry phosphorite are significantly higher than those of saturated phosphorite. As the load level increases, the shear cracks under both conditions gradually decrease. When the load level reaches 60–80%, the elliptical color of saturated phosphorite becomes more evident, and shear cracks show an increasing trend. This indicates that during unstable crack propagation phase, the presence of water affects the final failure pattern of phosphorite, a fact verified by Figure 9.

3.5. Energy Characteristics and Damage Mechanism under Dry and Saturated Conditions

The relationship between the releasable elastic and dissipated energy under uniaxial compression loading is shown in Figure 12. The area enclosed by the stress–strain curve and the unloaded elastic modulus in Figure 13 indicates dissipated energy (U_d), signifying the energy consumed when damage and plastic deformation occur. The shadow area indicates releasable elastic energy (U_e), and this part of the energy is the elastic energy that can be released after unloading. Since only the axial stress participates in the entire test process, the strain energy of each part can be calculated as:

$$U = \int_0^{\varepsilon} \sigma d\varepsilon, \tag{2}$$

$$U^e = \frac{1}{2}\sigma\varepsilon^e, \tag{3}$$

$$U^d = \int_0^{\varepsilon} \sigma d\varepsilon - \frac{\sigma^2}{2E_0}, \tag{4}$$

where ε is the strain during the entire loading process, ε^e is elastic strain, σ is stress and E_0 is initial elastic modulus.

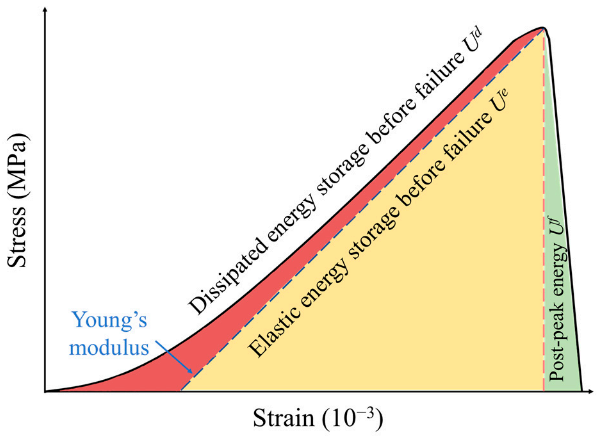

Figure 12. Diagram of quantitative relationship between dissipated energy and releasable elastic strain energy.

Figure 13 shows the energy evolution of phosphorite during the loading process. The values of U^e/U at the peak of dry and saturated samples are 0.803 and 0.798, respectively; U^d/U values are 0.197 and 0.202, respectively. This indicates that most of the strain energy absorbed by dry and saturated samples before peak in uniaxial compression is releasable, and that the proportion of dissipated energy consumed by internal damage and plastic deformation is small. However, the strain energy consumed by saturated phosphorite is significantly greater than that of dry phosphorite. Compared to dry samples, the stored strain energy in saturated phosphorite is significantly reduced. This indicates that water is conducive to reducing the release rate of strain energy when rock burst occurs. The U^d/U^e values (correction value of brittleness index defined by M. Aubertin [56]) of dry and saturated samples are 0.208 and 0.294, respectively. This indicates that the plastic deformation before the peak of saturated samples under uniaxial compression is greater than that of dry samples.

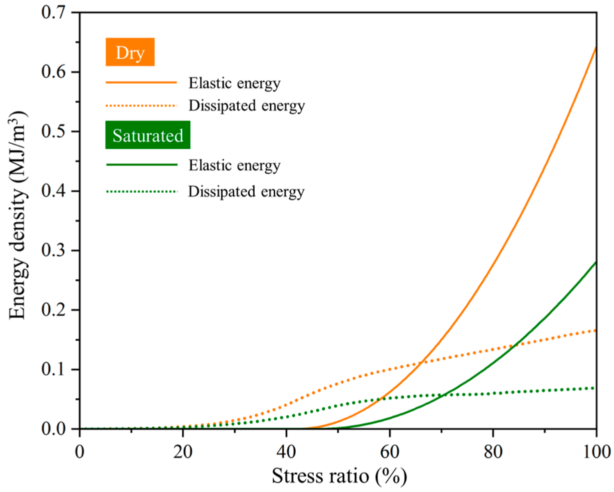

Figure 13. Energy evolution versus stress ratio before peak stress.

4. Discussion

The mechanism of watering to prevent rockburst is discussed from both macro and micro perspectives in this section. The mechanism diagram is shown in Figure 14. From a macro perspective, the drilling and blasting method is commonly used in the deep underground mining of phosphorite. The blasting load and transient unloading of rock mass lead to the adjustment of the excavation boundary stress, which is concentrated near the working face. However, watering the working face reduces the elastic modulus of the zone near the working face, thereby relocating the stress concentration zone away from the working face [43].

From a micro perspective, according to the fracturing results of lab tests, it can be concluded that more microcracks occur in the saturated phosphorite. This is due to the fact that saturation causes a stress-releasing effect on the working face during the process of stress adjustment after blasting, resulting in the transfer of stress. The generation and propagation mechanisms of microcracks can be divided into two categories depending on whether they factor in a crack's relationship with load. One category is load-dependent and includes factors such as the change in pore water pressure, the flow of pore water and the lubricating effect of the bound water film. When the load state of saturated phosphorite changes, the rock skeleton deforms and the pore space is compressed or stretched. When the pore space is smaller than the volume of free water in the pore, the compressed water tends to flow due to its incompressibility. In the pore networks with poor connectivity, the compression of pore water can lead to an increase in pore water pressure. For pores, the effect of internal water pressure is equivalent to the effect of outward tensile stress, which will intensify the concentration of tensile stress at the ends of pores (cracks), thereby promoting the propagation of cracks. The above microscopic processes have the potential to lead to the attenuation of the macroscopic mechanical properties of rocks. In pore networks with good levels of connectivity, the flow of pressurized pore water can lead to a redistribution of water pressure (from a high-pressure zone to a low-pressure zone), the weakening the local concentration of pore water pressure and the application of a hydrodynamic pressure to the rock skeleton, each of which has the potential to reduce the deformation resistance of a rock skeleton. This process can explain the reduction in rock elastic modulus at the macro level. The other category is load-independent and includes the hydration of clay minerals and the dissolution of soluble minerals. Phosphorite contains a small amount of hydromica, leading to interlayer expansion and intergranular expansion. Under the constraint of the rock skeleton, an expansion force is generated which acts on the rock skeleton [47,57]. If the expansion force is large enough, it will lead to the propagation of existing cracks and the generation of new cracks. On the other hand, dolomite in phosphorite belongs to a soluble mineral; its presence can directly lead to the loss of rock skeleton material and a change in pore shape during the water absorption process.

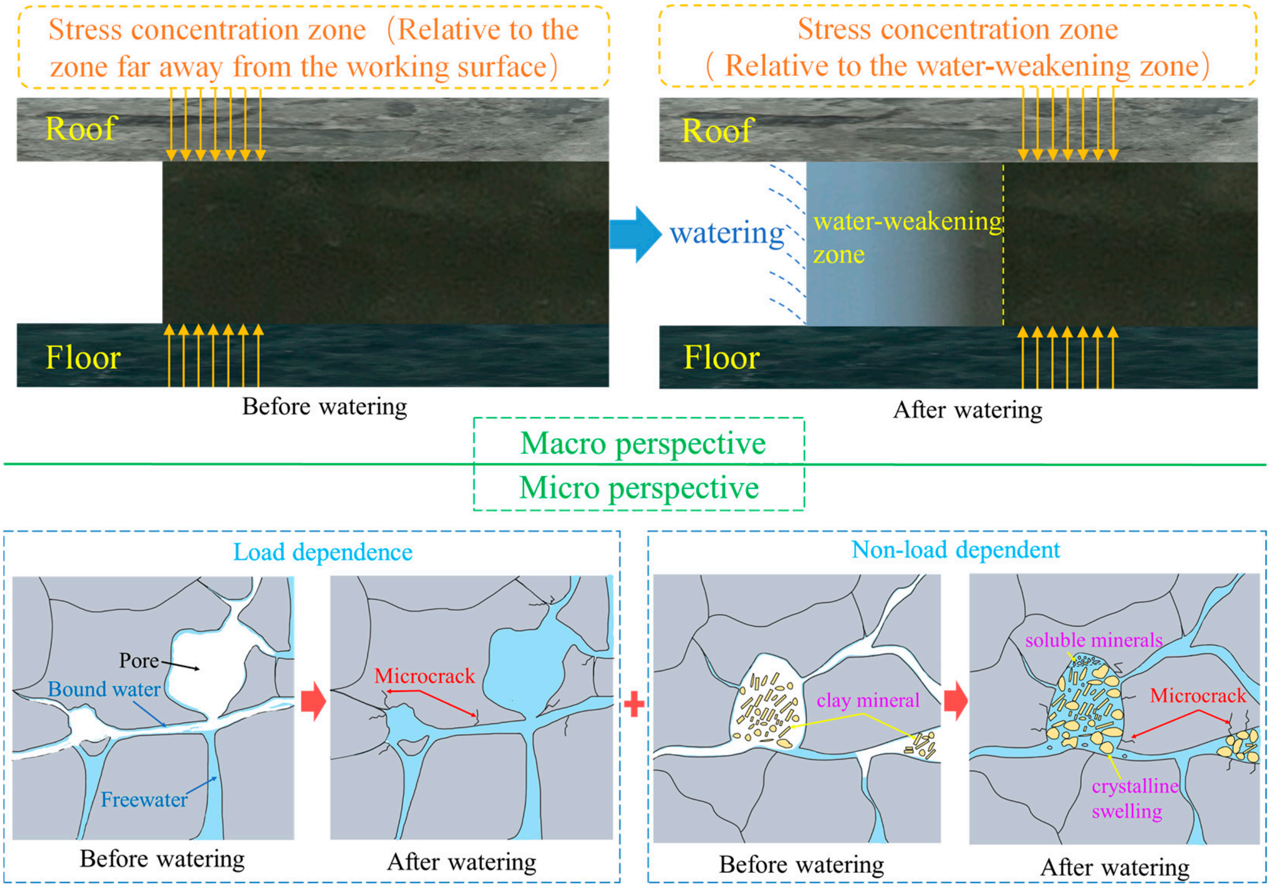

Figure 14. Brief diagram: the mechanism of preventing rock burst by watering is discussed from both macro and micro levels.

5. Conclusions

Water weakens the uniaxial compressive strength and Young's modulus, while also reducing the elastic strain energy storage capacity. Analyzing the fracturing process and results of phosphorite shows that both dry and saturated samples are violently broken into multiple fragments, although saturated samples are broken into a significantly larger number of small fragments and powders after fracturing than dry samples. The fracturing of both dry and saturated samples is dominated by tension cracks; however, the presence of bound water films leads to the development of a greater number of shear cracks in saturated phosphorite.

The mechanism of preventing rockburst via watering is discussed from both macro and micro perspectives. From a macro perspective, we can assert that watering reduces Young's modulus of the zone near the working face with the effect of keeping the stress concentration zone away from it. From a micro perspective, a greater quantity of microcracks occur in the saturated phosphorite after watering, resulting in a stress-releasing effect on the working face and leading to stress transfer. The generation and propagation mechanisms of microcracks can be divided into two categories on the basis of whether they depend on load. The category of load-dependent cracks is influenced by the change in pore water pressure, the flow of pore water and the lubricating effect of a bound water film. The load-independent category of cracks is altered by the hydration of clay minerals (hydromica in phosphorite) and the dissolution of soluble minerals (dolomite in phosphorite).

Most rockbursts in phosphorite mines are immediate and usually occur between 2 and 8 h of blasting. Therefore, future research should determine how to quickly saturate the working face and roof with water and generally optimize the watering method. The results could offer guidance for setting up indicators to evaluate the effectiveness of watering for rockburst prevention.

Author Contributions: Conceptualization, M.W.; methodology, Y.Y. and Q.W.; software, Z.Z.; investigation, Y.L. and W.L.; writing—original draft preparation, M.W.; writing—review and editing, M.W. and Y.Y.; visualization, M.W.; supervision, Q.W.; funding acquisition, M.W., Y.Y. and Q.W. All authors have read and agreed to the published version of the manuscript.

Funding: The authors gratefully acknowledge the support of the Key RD projects in Hubei Province (grant number 2020BCA082) and the Key RD projects in Hubei Province (grant number SJZX20211004).

Institutional Review Board Statement: Not applicable.

Informed Consent Statement: Not applicable.

Data Availability Statement: All data used in the article and relevant conclusions obtained therefrom are included in this article.

Acknowledgments: The authors gratefully acknowledge test equipment and technical support provided by the employees from the Yichang Dongda Co., Ltd.

Conflicts of Interest: The authors declare that they have no known competing financial interest or personal relationship that could have appeared to influence the work reported in this paper.

References

1. Ortlepp, W.D.; Stacey, T.R. Rockburst Mechanisms in Tunnels and Shafts. *Tunn. Undergr. Space Technol.* **1994**, *91*, 59–65. [CrossRef]
2. Kaiser, P.K.; Cai, M. Design of rock support system under rockburst condition. *J. Rock Mech. Geotech. Eng.* **2012**, *4*, 215–227. [CrossRef]
3. Mazaira, A.; Konicek, P. Intense rockburst impacts in deep underground constructions and their prevention. *Can. Geotech. J.* **2015**, *52*, 1426–1439. [CrossRef]
4. Feng, X.T.; Liu, J.P.; Chen, B.R.; Xiao, Y.X.; Feng, G.L.; Zhang, F.P. Monitoring, Warning, and Control of Rockburst in Deep Metal Mines. *Engineering* **2017**, *3*, 538–545. [CrossRef]
5. Li, X.B.; Zhou, Z.L.; Lok, T.S.; Hong, L.; Yin, T.B. Innovative testing technique of rock subjected to coupled static and dynamic loads. *Int. J. Rock Mech. Min. Sci.* **2008**, *45*, 739–748. [CrossRef]
6. Li, X.B.; Cao, W.; Tao, M.; Zhou, Z.; Chen, Z. Influence of unloading disturbance on adjacent tunnels. *Int. J. Rock Mech. Min. Sci.* **2016**, *84*, 10–24. [CrossRef]
7. Li, H.B.; Xia, X.; Li, J.C.; Zhao, J.; Liu, B.; Liu, Y.Q. Rock damage control in bedrock blasting excavation for a nuclear power plant. *Int. J. Rock Mech. Min. Sci.* **2011**, *48*, 210–218.
8. Li, X.B.; Du, K.; Li, D.Y. True triaxial strength and failure modes of cubic rock specimens with unloading the minor principal stress. *Rock Mech. Rock Eng.* **2015**, *48*, 2185–2196. [CrossRef]
9. He, S.Q.; Song, D.Z.; He, X.Q.; Chen, J.Q.; Ren, T.; Li, Z.L.; Qiu, L.M. Coupled mechanism of compression and prying-induced rock burst in steeply inclined coal seams and principles for its prevention. *Tunn. Undergr. Space Technol.* **2020**, *98*, 103327. [CrossRef]
10. Cai, W.; Dou, L.M.; Gong, S.Y.; Li, Z.L.; Yuan, S. Quantitative analysis of seismic velocity tomography in rock burst hazard assessment. *Nat. Hazards* **2015**, *75*, 2453–2465. [CrossRef]
11. Li, X.B.; Gong, F.Q.; Tao, M.; Dong, L.J.; Du, K.; Ma, C.D.; Zhou, Z.L.; Yin, T. Failure mechanism and coupled static-dynamic loading theory in deep hard rock mining: A review. *J. Rock Mech. Geotech. Eng.* **2017**, *9*, 767–782. [CrossRef]
12. Deng, J.; Gu, D.S. Buckling mechanism of pillar rockbursts in underground hard rock mining. *Géoméch. Geoengin.* **2018**, *13*, 168–183. [CrossRef]
13. Wang, G.F.; Li, G.; Dou, L.M.; Mu, Z.L.; Gong, S.Y.; Cai, W. Applicability of energy-absorbing support system for rockburst prevention in underground roadways. *Int. J. Rock Mech. Min. Sci.* **2020**, *132*, 104396. [CrossRef]
14. Yan, P.; Zhao, Z.G.; Lu, W.B.; Fan, Y.; Chen, X.R.; Shan, Z.G. Mitigation of rock burst events by blasting techniques during deep-tunnel excavation. *Eng. Geol.* **2015**, *188*, 126–136. [CrossRef]
15. Liu, X.F.; Xu, G.; Zhang, C.; Kong, B.; Qian, J.F.; Zhu, D.; Wei, M.Y. Time Effect of Water Injection on the Mechanical Properties of Coal and Its Application in Rockburst Prevention in Mining. *Energies* **2017**, *10*, 1783. [CrossRef]
16. He, M.C.; Ren, F.Q.; Liu, D.Q. Rockburst mechanism research and its control. *Int. J. Min. Sci. Technol.* **2018**, *28*, 829–837. [CrossRef]
17. Wasantha, P.L.P.; Ranjith, P.G. Water-weakening behavior of Hawkesbury sandstone in brittle regime. *Eng. Geol.* **2014**, *178*, 91–101. [CrossRef]

18. Ciantia, M.O.; Castellanza, R.; di Prisco, C. Experimental study on the water-induced weakening of calcarenites. *Rock Mech. Rock Eng.* **2015**, *48*, 441–461. [CrossRef]
19. Song, D.Z.; Wang, E.Y.; Liu, Z.T.; Liu, X.F.; Shen, R.X. Numerical simulation of rock-burst relief and prevention by water-jet cutting. *Int. J. Rock Mech. Min. Sci.* **2014**, *70*, 318–331. [CrossRef]
20. Xie, N.; Tang, H.M.; Yang, J.B.; Jiang, Q.H. Damage Evolution in Dry and Saturated Brittle Sandstone Revealed by Acoustic Characterization Under Uniaxial Compression. *Rock Mech. Rock Eng.* **2022**, *55*, 1303–1324. [CrossRef]
21. Yilmaz, I. Influence of water content on the strength and deformability of gypsum. *Int. J. Rock Mech. Min. Sci.* **2010**, *47*, 342–347. [CrossRef]
22. Hawkins, A.B.; McConnell, B.J. Sensitivity of sandstone strength and deformability to changes in moisture content. *Q. J. Eng. Geol.* **1992**, *25*, 115–130. [CrossRef]
23. Vásárhelyi, B.; Ván, P. Influence of water content on the strength of rock. *Eng. Geol.* **2006**, *84*, 70–74. [CrossRef]
24. Luo, D.N.; Xie, Y.Q.; Liu, S.H.; Su, G.S. Experimental Study on the Effects of Water Saturation on the Microseismic and Acoustic Emission Characteristics of Sandstone in Different Stress States. *Rock Mech. Rock Eng.* **2022**, *55*, 6583–6603. [CrossRef]
25. Huang, X.; Wang, T.; Luo, Y.; Guo, J. Study on the Influence of Water Content on Mechanical Properties and Acoustic Emission Characteristics of Sandstone: Case Study from China Based on a Sandstone from the Nanyang Area. *Sustainability* **2023**, *15*, 552. [CrossRef]
26. Wen, G.; Hu, J.; Wu, Y.; Zhang, Z.X.; Xu, X.; Xiang, R. Mechanical Properties and Failure Behavior of Dry and Water-Saturated Foliated Phyllite under Uniaxial Compression. *Materials* **2022**, *15*, 8962. [CrossRef] [PubMed]
27. Si, X.F.; Gong, F.Q. Strength-weakening effect and shear-tension failure mode transformation mechanism of rockburst for fine-grained granite under triaxial un-loading compression. *Int. J. Rock Mech. Min. Sci.* **2020**, *131*, 104347. [CrossRef]
28. Gu, H.; Tao, M.; Li, X.; Momeni, A.; Cao, W. The effects of water content and external incident energy on coal dynamic behaviour. *Int. J. Rock Mech. Min. Sci.* **2019**, *123*, 104088. [CrossRef]
29. Erguler, Z.A.; Ulusay, R. Water-induced variations in mechanical properties of clay-bearing rock. *Int. J. Rock Mech. Min. Sci.* **2009**, *46*, 355–370. [CrossRef]
30. Waza, T.; Kurita, K.; Mizutani, H. The effect of water on the subcritical crack growth in silicate rocks. *Tectonophysics* **1980**, *67*, 25–34. [CrossRef]
31. Nara, Y.; Morimoto, K.; Hiroyoshi, N.; Yoneda, T.; Kaneko, K.; Benson, P.M. Influence of relative humidity on fracture toughness of rock: Implications for subcritical crack growth. *Int. J. Solids Struct.* **2012**, *49*, 2471–2481. [CrossRef]
32. Wong, L.N.Y.; Maruvanchery, V.; Liu, G. Water effects on rock strength and stiffness degradation. *Acta Geotech.* **2016**, *11*, 713–737. [CrossRef]
33. Fowkes, N. Rockbursts Mud and Plastic. In Proceedings of the 19th International Congress on Modelling and Simulation, Modelling and Simulation Society of Australia and New Zealand, Perth, Australia, 12–16 December 2011; pp. 304–310.
34. Xu, N.W.; Li, T.B.; Dai, F.; Zhang, R.; Tang, C.A.; Tang, L.X. Microseismic Monitoring of Strainburst Activities in Deep Tunnels at the Jinping II Hydropower Station, China. *Rock Mech. Rock Eng.* **2016**, *49*, 981–1000. [CrossRef]
35. Lipponen, A.; Airo, M.L. Linking regional-scale lineaments to local-scale fracturing and groundwater inflow into the Paijanne water-conveyance tunnel, Finland. *Near Surf. Geophys.* **2006**, *4*, 97–111. [CrossRef]
36. Perello, P.; Baietto, A.; Burger, U.; Skuk, S. Excavation of the Aica-Mules pilot tunnel for the Brenner base tunnel: Information gained on water inflows in tunnels in granitic massifs. *Rock Mech. Rock Eng.* **2014**, *47*, 1049–1071. [CrossRef]
37. Frid, V. Electromagnetic radiation method water-infusion control in rockburst-prone strata. *J. Appl. Geophys.* **2000**, *43*, 5–13. [CrossRef]
38. Xu, H.C.; Lai, X.P.; Shan, P.F.; Yang, Y.B.; Zhang, S.; Yan, B.X.; Zhang, Y.; Zhang, N. Energy dissimilation characteristics and shock mechanism of coal-rock mass induced in steeply-inclined mining: Comparison based on physical simulation and numerical calculation. *Acta Geotech.* **2023**, *18*, 843–864. [CrossRef]
39. Liu, B.B.; Zhao, F.J.; Wu, Q.H.; Wang, B.; Tan, J.N.; Feng, T. Mesomechanism of effects of water on strain rockburst prevention. *Adv. Civ. Eng.* **2021**, *2021*, 6631342. [CrossRef]
40. Liu, X.X.; Liang, Z.Z.; Zhang, Y.B.; Liang, P.; Tian, B.Z. Experimental study on the monitoring of rockburst in tunnels under dry and saturated conditions using AE and infrared monitoring. *Tunn. Undergr. Space Technol.* **2018**, *82*, 517–528. [CrossRef]
41. Luo, Y. Influence of water on mechanical behavior of surrounding rock in hard-rock tunnels: An experimental simulation. *Eng. Geol.* **2020**, *277*, 105816. [CrossRef]
42. Luo, Y.; Gong, F.Q.; Zhu, C.Q. Experimental investigation on stress-induced failure in D-shaped hard rock tunnel under water-bearing and true triaxial compression conditions. *Bull. Eng. Geol. Environ.* **2022**, *81*, 76. [CrossRef]
43. Cai, X.; Cheng, C.Q.; Zhou, Z.L.; Konietzky, H.; Song, Z.Y.; Wang, S.F. Rock mass watering for rock-burst prevention: Some thoughts on the mechanisms deduced from laboratory results. *Bull. Eng. Geol. Environ.* **2021**, *80*, 8725–8743. [CrossRef]
44. Keneti, A.; Sainsbury, B.A. Review of published rockburst events and their contributing factors. *Eng. Geol.* **2018**, *246*, 361–373. [CrossRef]
45. Masoud, G.; Korosh, S.; Mostafa, S.; Reza, M. A critical review on the developments of rock support systems in high stress ground conditions. *Int. J. Min. Sci. Technol.* **2020**, *30*, 555–572.
46. Song, Z.; Konietzky, H.; Cai, X. Modulus degradation of concrete exposed to compressive fatigue loading: Insights from lab testing. *Struct. Eng. Mech.* **2021**, *78*, 281–296.

47. Laird, D.A. Influence of layer charge on swelling of smectites. *Appl. Clay Sci.* **2006**, *34*, 74–87. [CrossRef]
48. Carpinteri, A.; Corrado, M.; Lacidogna, G. Heterogeneous materials in compression: Correlations between absorbed, released and acoustic emission energies. *Eng. Fail. Anal.* **2013**, *33*, 236–250. [CrossRef]
49. Rodríguez, P.; Celestino, T.B. Application of acoustic emission monitoring and signal analysis to the qualitative and quantitative characterization of the fracturing process in rocks. *Eng. Fract. Mech.* **2019**, *210*, 54–69. [CrossRef]
50. Shiotani, T.; Ohtsu, M.; Ikeda, K. Detection and evaluation of AE waves due to rock deformation. *Constr. Build. Mater.* **2001**, *15*, 235–246. [CrossRef]
51. Wang, H.; Liu, D.; Cui, Z.; Cheng, C.; Jian, Z. Investigation of the fracture modes of red sandstone using XFEM and acoustic emissions. *Theor. Appl. Fract. Mech.* **2016**, *85*, 283–293. [CrossRef]
52. Prem, P.R.; Murthy, A.R. Acoustic emission monitoring of reinforced concrete beams subjected to four-point-bending. *Appl. Acoust.* **2017**, *117*, 28–38. [CrossRef]
53. Sagar, R.V.; Srivastava, J.; Singh, R.K. A probabilistic analysis of acoustic emission events and associated energy release during formation of shear and tensile cracks in cementitious materials under uniaxial compression. *J. Build. Eng.* **2018**, *20*, 647–662. [CrossRef]
54. Vidya Sagar, R. Verification of the applicability of the Gaussian mixture modelling for damage identification in reinforced concrete structures using acoustic emission testing. *J. Civ. Struct. Health Monit.* **2018**, *8*, 395–415. [CrossRef]
55. Yang, J.; Zhao, K.; Yu, X.; Yan, Y.; He, Z.; Lai, Y.; Zhou, Y. Crack classification of fiber-reinforced backfill based on Gaussian mixed moving average filtering method. *Cem. Concr. Compos.* **2022**, *134*, 104740. [CrossRef]
56. Aubertin, M.; Gillde, E.; Simon, R. On the use of the brittleness index modified (BIM) to estimate the post-behavior of rock. In *1′ North American Rock Mechanics Symposium Rotterdam*; Balkema, A.A., Ed.; OnePetro: Richardson, TX, USA, 1994; pp. 945–952.
57. Schult, A.; Shi, G. Hydration swelling of crystalline rocks. *Geophys. J. Int.* **1997**, *131*, 179–186. [CrossRef]